ADVANCED FUNCTIONAL MATERIALS
www.afm-journal.de

Solid State Fluorination on the Minute Scale: Synthesis of $WO_{3-x}F_x$ with Photocatalytic Activity

*Martin Alexander Lange, Yaşar Krysiak, Jens Hartmann, Georg Dewald, Giacomo Cerretti, Muhammad Nawaz Tahir, Martin Panthöfer, Bastian Barton, Tobias Reich, Wolfgang G. Zeier, Mihail Mondeshki, Ute Kolb, and Wolfgang Tremel**

Dedicated with admiration to Prof. Arndt Simon on the occasion of his 80 birthday

Solid state reactions are notoriously slow, because the rate-limiting step is diffusion of atoms or ions through reactant, intermediate, and product crystalline phases. This requires days or even weeks of high temperature treatment, consuming large amounts of energy. Metal oxides are particularly difficult to react, because they have high melting points. The study reports a high-speed solid state fluorination of WO_3 with Teflon to the oxyfluorides $WO_{3-x}F_x$ on a minute (<10 min) scale by spark plasma sintering, a technique that is used typically for a high-speed consolidation of powders. Automated electron diffraction analysis reveals an orthorhombic ReO_3-type structure of $WO_{3-x}F_x$ with F atom disorder as demonstrated by ^{19}F magic angle spinning nuclear magnetic resonance spectroscopy. The potential of this new approach is demonstrated by the following results. i) Mixed- valent tungsten oxide fluorides $WO_{3-x}F_x$ with high F content ($0 < x < 0.65$) are obtained as metastable products in copious amounts within minutes. ii) The spark plasma sintering technique yields $WO_{3-x}F_x$ nanoparticles with high photocatalytic activity, whereas the corresponding bulk phases obtained by conventional solid-state (ampoule) reactions have no photocatalytic activity. iii) The catalytic activity is caused by the microstructure originating from the processing by spark plasma sintering.

1. Introduction

Energy efficiency, sustainability, and economic viability are becoming increasingly important for materials manufacturing in industry. Microwave methods[1,2] allow rapid materials processing with improved energy efficiency and reduced equipment costs. Similarly, spark plasma sintering (SPS) has become a state-of-the-art method,[3,4] where a uniaxial force and a pulsed electric field (dc current) allow a high speed consolidation of polycrystalline powders.[9,10] The detailed mechanism of SPS reactions is still far from being understood,[3,4] but the primary effect of the current in the sintering process is likely to be Joule heating. Other non-thermal effects may contribute to the solid-state reaction kinetics. This may alter the nature of the final product.[4–8] Although, SPS is an important form-giving process, its application for the synthesis of new materials is still in its infancy.[11–13]

M. A. Lange, J. Hartmann, Dr. G. Cerretti, Dr. M. Panthöfer, M. Mondeshki, Dr. U. Kolb, Prof. W. Tremel
Institut für Anorganische Chemie und Analytische Chemie
Johannes Gutenberg-Universität Mainz
Duesbergweg 10–14, D-55128 Mainz, Germany
E-mail: tremel@uni-mainz.de

Dr. Y. Krysiak, Dr. U. Kolb
Institut für Angewandte Geowissenschaften
Technische Universität Darmstadt
Schnittspahnstraße 9, 64287 Darmstadt, Germany

The ORCID identification number(s) for the author(s) of this article can be found under https://doi.org/10.1002/adfm.201909051.

DOI: 10.1002/adfm.201909051

Dr. Y. Krysiak
Department of Structure Analysis
Institute of Physics
Czech Academy of Sciences
Cukrovarnická 10/112, 162 00 Prague, Czech Republic

G. Dewald, Dr. W. G. Zeier
Justus-Liebig-University Giessen
Physikalisch-Chemisches Institut
Heinrich-Buff-Ring 17, D-35392 Giessen, Germany

Dr. M. N. Tahir
Chemistry Department
King Fahd University of Petroleum and Materials
Dharan 31261, P.O. Box 5048, Kingdom of Saudi Arabia

Dr. B. Barton
Fraunhofer LBF
Division Plastics
Schlossgartenstr. 6, D-64289 Darmstadt, Germany

Prof. T. Reich
Institut für Kernchemie
Johannes Gutenberg-Universität Mainz
Strassmannweg 2, D-55128 Mainz, Germany

In the past, a variety of fluorination techniques have been devised for fluoride "doping" or to synthesize oxyfluorides. Many of them requires fluorine gas, reactive fluorides, or hydrogen fluoride as toxic and corrosive fluorine sources that require special equipment and handling techniques.[14–16] A synthesis of $WO_{3-x}F_x$ by heating WO_3 with HF under extreme conditions in sealed gold ampoules has been reported.[17] High-temperature approaches using binary fluorides (like MF_2 or MF_3 (M = alkaline-earth or lanthanide metal) have limitations because of the stability of the starting compounds compared to the intended products.[18] Therefore, alternate fluorination routes have been developed for obtaining oxyfluorides.[19–24]

Fluorination using a powder of the fluorinated polymers as a source of fluorine in a reductive fluorination process relies on their solid form, chemical stability at room temperature and their relatively low decomposition temperature compared with most inorganic compounds.[21–24] This allows to perform a reductive fluorination of oxides easily and safely. The convenience and usability of this method for the synthesis of superconducting $WO_{3-x}F_x$ has already been demonstrated.[22] $WO_{3-x}F_x$ has been synthesized with different fluorine contents, but photocatalytic activity similar as for the related Magneli phases[25] has not been reported. We report a new SPS approach on a minute scale for the rapid fluorination of WO_3 with polytetrafluorethylene (PTFE) to the oxy-fluorides $WO_{3-x}F_x$ with high photocatalytic activity in copious amounts. These solid-state reactions were complete several minutes and lead, depending on the ratio of the starting compounds, to the formation of oxyfluorides $WO_{3-x}F_x$ ($0 < x < 0.6$) with colors ranging from light green to blue as the fluorine content increased. This systematic color change during fluorination reaction is the same as that generally observed in tungsten bronzes and indicates mixed-valency of the tungsten atoms through charge carriers introduced into the system by chemical reduction. The reaction is diffusion controlled as seen from the presence of two phases in ex situ X-ray powder diffraction, in automated diffraction analysis (ADT) and by the shift of the reaction front from the periphery to the core of the tungsten oxide grains in transmission electron microscopy (TEM). This indicates that fluorine diffuses into the WO_3 particles prepared by ball milling. At an intermediate stage, a noncompletely reacted WO_3 core is surrounded by a $WO_{3-x}F_x$ shell. At 450 °C, the reaction proceeds via monoclinic and orthorhombic intermediates, which have not been reported before. At 550 °C, the reaction product for $x = 0.10$ contains an orthorhombic main phase and a cubic side phase (15%). For $x = 0.3$–0.4 the cubic phase is the majority phase with minor (5%) contribution of the orthorhombic phase. The cubic phase exhibits F atom disorder as demonstrated by ^{19}F magic angle spinning nuclear magnetic resonance (MAS-NMR) experiments.[26,27]

X-ray photoelectron spectroscopy (XPS) revealed that SPS-prepared $WO_{3-x}F_x$ contained mixed-valent W^{6+}/W^{5+}. $WO_{3-x}F_x$ shows photocatalytic activity, whereas conventionally prepared $WO_{3-x}F_x$ is photocatalytically inactive. The conceptual advancement of this new synthetic approach toward functional nanomaterials lies in the combination of the fluorination with fluorinated polymers and spark plasma sintering, typically used in ceramics and alloys fields to sinter while limiting grain growth. SPS, reported for incorporating carbon into sol–gel-derived microstructured oxide matrixes,[28,29] is used for the first time for the fast one-pot synthesis of oxyfluorides. It yields large monoliths of metal oxyfluoride nanopowders. The photocatalytic activity is strongly enhanced through the SPS processing. This suggests that new photocatalytic compounds based on cheap, air-stable, and environmentally benign elements might be discovered by SPS processing from polymer scrap.[30]

2. Results and Discussion

2.1. SPS Synthesis and Chemical Analysis

$WO_{3-x}F_x$ was synthesized using SPS (**Figure 1**A). Prior to the reaction, the components WO_3 and PTFE were mixed for 30×10 min with 10 min intermissions at 740 rpm in a planetary ball mill using 8 g of grinding balls (ZrO_2, 1 mm diameter) and ≈10 mL of ethanol as dispersion medium. No reaction occurred during ball milling as judged by powder X-ray diffraction and ^{19}F-MAS NMR. In a second, pyrometer-controlled heating step the reactant mixture was SPS treated using the temperature profile shown in Figure 1B. After preparation, the products typically contained phase mixtures with densities ≥90% of the calculated theoretical density. In the first steps, the samples were heated to 400, 450, 500, 550, and 600 °C, and

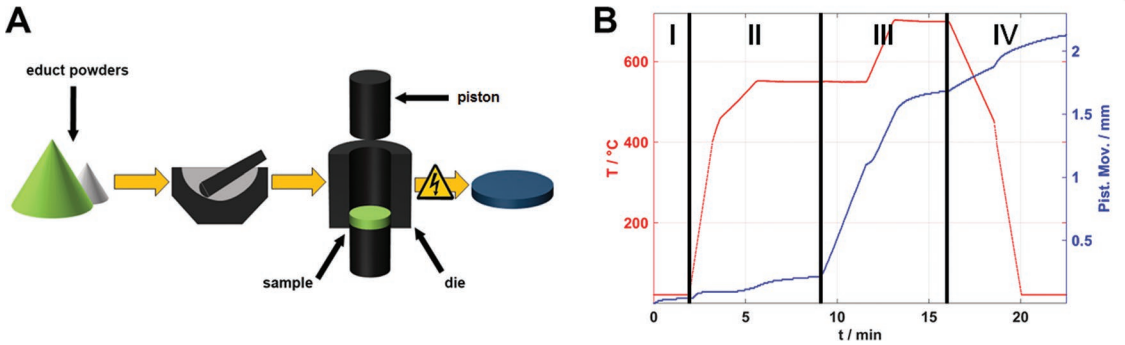

Figure 1. A) Illustration of the synthesis procedure. Different from the conventional approach, reaction and consolidation take place simultaneously. Precursor materials: WO_3 and PTFE. B) Temperature profile (red) and piston movement/densification (blue) during the SPS process. Capital letters indicate different segments of the process: I) Evacuation of reaction chamber and first compression, II) start of reaction by heating to 550 °C and dwelling for 4 min, III) increase of pressure at 550 °C from 19 to 50 MPa and second heating step at 700 °C, IV) sample cooling.

the reactions were quenched immediately after reaching the set-point temperatures. Higher temperatures did not accelerate the reaction, because unreacted PTFE decomposition products are lost, which leads to incomplete reaction. Similarly, high pressures lead to losses of PTFE decomposition products. Therefore, a relatively low pressure (19 MPa) was chosen for the synthesis. Above ≈750 °C, F-containing products were lost, and the formation of reduced tungsten oxides was observed. Thus, the sintering time was varied between 2 and 6 min at 550 and at 600 °C. The main reaction came to completion during this short heating segment.

The reaction of WO_3 with polytetrafluoroethylene is assumed to occur at the gas–solid interface, since PTFE starts to decompose slowly at 360 °C.[31] Thermal analysis showed the thermal decomposition to be complete above 400 °C, the main decomposition products under vacuum conditions being the C_2F_4 monomer.[32,33] In the SPS experiments, C_2F_4 resulting from the thermal decomposition of the fluorinated polymers is likely diffuse through the grain boundaries of the WO_3 sample at the reaction temperature of 550 °C. This is indicated by the need of ball-milling for high degrees of fluorination and the presence of PTFE flakes around the WO_3 particles at high PTFE/WO_3 ratios (Figure S1, Supporting Information). For unsufficient mixing of the WO_3 and PTFE precursors lower degrees of fluorination were observed. In addition, a thin white deposit of PTFE was observed at the cold side of the pressing tools after the SPS reaction. Still, the detailed fluorination mechanism remains unclear because i) the state of matter of C_2F_4 under the reaction conditions (19 MPa, 550 °C) is not clear, ii) follow-up reactions of C_2F_4 may form fluorocarbon oligomers depending on reaction temperature and pressure. Increasing the applied pressure to 50 MPa after 4 min at 550 °C and performing a second heating step for 3 min at 700 °C allowed to further increase the fluorine content up to $x \approx 0.6$.

A conventional synthesis of $WO_{3-x}F_x$ was carried out as control experimentals using the same ball-milled precursor mixtures in evacuated quartz tubes that were sintered at 550 °C for 36 h. The reaction was performed with ≈500 mg of mixture in quartz tubes having a volume of ≈35 cm^3.

2.2. Phase Analysis

The phase compositions of all samples were determined by powder X-ray diffraction (PXRD) and TEM. The fluorine content of phase pure samples based on PXRD was determined electrochemically with a F^--ion selective electrode (for details see the Experimental Section). The nominal and true F/W ratios are compiled in **Table 1**. Compositions determined by potentiometry will be used in the sequel. The true fluorine content increases with increasing nominal fluorine content in $WO_{3-x}F_x$, although not in a linear fashion. An excess of fluorinated polymer is needed to achieve high fluorine contents in $WO_{3-x}F_x$. Heat treatment of SPS samples in air to remove carbon residues after the reaction did not lead to changes of the phase composition.

The SPS synthesis of $WO_{3-x}F_x$ yielded significantly higher degrees of fluorination than conventional methods using the same ball-milled precursor mixture, because heating to $T > 550$ °C in quartz ampules led to loss of fluorine or even the formation of reduced tungsten oxides.[22–24] In SPS, the increase of the reaction temperature to 600 °C still led to an increase of the fluorine content (indicated by an increase of the lattice parameter of the cubic unit $WO_{3-x}F_x$ cell for large PTFE excess), while samples dwelled at 600 °C for more than 10 min showed a lower fluorine content (Figure S2, Supporting Information). Optimization of the reaction protocol led to the temperature program shown Figure 1B. After a first reaction step at 550 °C, fast heating and short dwelling at 700 °C for 3 min allowed the synthesis of highly fluorinated samples (up to $x = 0.6$) while only negligible amounts of WO_2 were formed as a side phase (phase purity > 98%). Increasing the annealing temperature and time resulted in additional side reactions of PTFE and decomposition products with graphite or C-containing decomposition products of PTFE. This led to a contamination of $WO_{3-x}F_x$ with several, nonidentified phases. This maximum fluorine content of $WO_{3-x}F_x$ is significantly higher than that obtained in conventional reactions in quartz ampoules,[22] and comparable to that of reactions with HF under high pressure ($x = 0.43$ in 48% aqueous HF, and $x = 0.66$ with anhydrous HF)[17] However, reductive fluorination in SPS reactions was much faster (5–9 min vs 24 h), and it can be upscaled easily to the kg range with appropriate dies.[4] In addition, it is much easier, cheaper and safer to carry out than reactions under high pressure with HF in gold ampoules.

Table 1. Calculated F/W ratios of orthorhombic and cubic $WO_{3-x}F_x$, determined potentiometrically with a F^- sensitive electrode. X_{nom} describes the F excess in the starting material, while X_{true} describes the ratios as determined by F^--selective potentiometric measurements.

Method	V/Z [Å]	X_{nom}	X_{true}	E_{gap} [eV]
SPS + 700 °C	55.85	1.5	0.60	3.51
SPS	53.25	0.15	0.10	3.31
Conventional ampoule reaction	55.48	1.0	0.42	3.37
Conventional ampoule reaction	53.35	0.1	0.08	3.20

X-ray diffraction (XRD) patterns of $WO_{3-x}F_x$ for different values of x (**Figure 2**A,B) showed that the crystal structure of $WO_{3-x}F_x$ depends on the fluorine content x. The XRD patterns of $WO_{3-x}F_x$ for $x = 0.10$ and $x = 0.6$ could be indexed based on orthorhombic (space group: *Pbcn*) and cubic (space group: $Pm\bar{3}m$) unit cells, respectively (vide infra). Crystallographic details and essential results of the Rietveld refinements[34,35] for SPS-prepared $WO_{3-x}F_x$ for $x = 0.10$ and $x = 0.60$ (refined compositions $WO_{2.90}F_{0.10}$ and $WO_{2.40}F_{0.60}$) are listed in **Tables 2** and **3** (conventionally prepared $WO_{2.92}F_{0.08}$ and $WO_{2.58}F_{0.42}$ in Figure S3, Supporting Information). A cubic $WO_{3-x}F_x$ phase with high fluorine content (0.17–0.66) has been reported before.[17,22] Since the crystal structure of orthorhombic $WO_{2.9}F_{0.1}$ was unknown, it was determined using a combination of ADT and PXRD (vide infra).

Analysis of the unit cell volume per number of tungsten atoms in the unit cell (obtained by Rietveld refinement) are in agreement with the fluorine content determined by fluoride ion selective potiometry assuming Vegard-behavior[36] of the fluorine substituted samples. It is difficult to determine the accurate content of lattice F and O by electron and X-ray diffraction only.

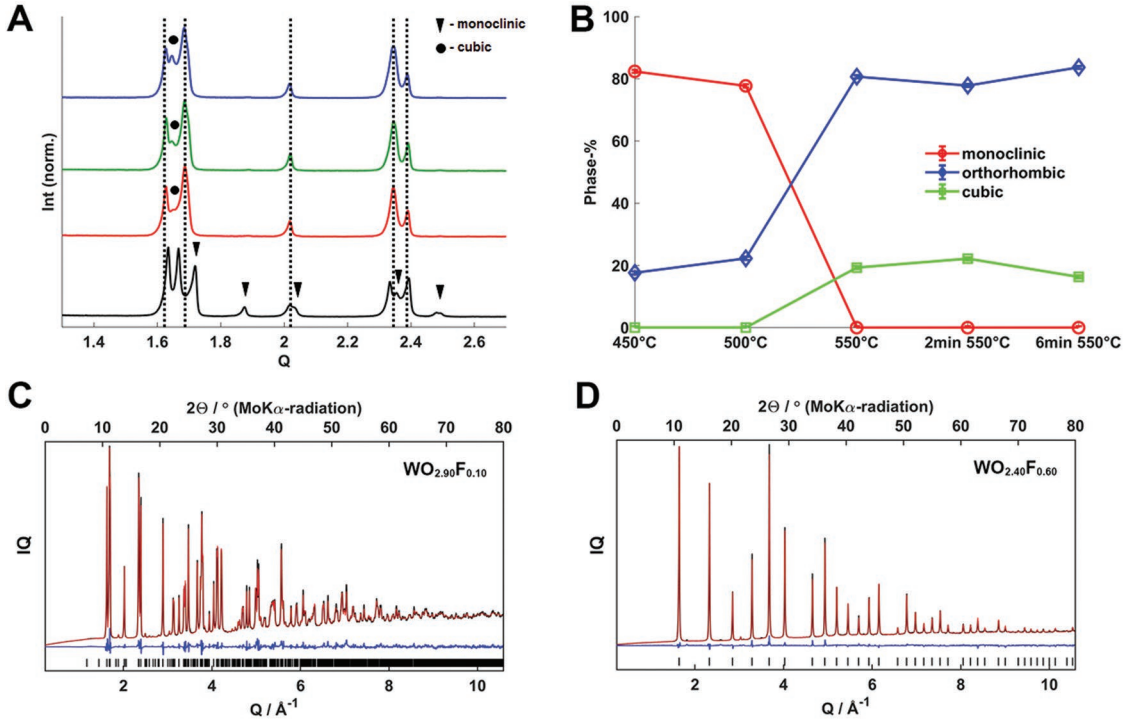

Figure 2. A) X-ray powder diffractograms of samples obtained by quenching the SPS reaction (F:W ratio of the starting material ≈0.15) at 500 °C (black line) and 550 °C (red line) with immediate cooling after heating, after 2 min at 550 °C (green line) and after 6 min at 550 °C (blue line) when the reaction was complete. Dotted lines indicate reflections of the orthorhombic phase. Circles indicate growing reflections belonging of the cubic phase, triangles indicate vanishing reflections of monoclinic tungsten trioxide. An increase of the fluorine content leads to a larger unit cell and causes the shift of the reflections. B) Analysis of the phase composition of the obtained samples at several stages of the reaction showing the gradual formation of i) orthorhombic and ii) cubic $WO_{3-x}F_x$. C,D) Rietveld refinements of SPS prepared $WO_{2.90}F_{0.10}$ and $WO_{2.40}F_{0.60}$ using X-ray powder data. A,B): $WO_{2.90}F_{0.10}$ (orthorhombic) and $WO_{2.40}F_{0.60}$ (cubic) prepared by SPS processing (R_{wp} = 3.75%/3.27%, gof = 2.02/1.54). Intensity weighted with *Q*-value.

2.3. Structure Determination of $WO_{2.90}F_{0.10}$ and $WO_{2.40}F_{0.60}$ by ADT

Neither structural solution nor refinement was possible for SPS-$WO_{2.90}F_{0.10}$ with the reported indexing.[22] Electron diffraction has the advantage that single crystal diffraction data may be obtained from nanometer-sized regions. It is also sensitive to superlattice reflections arising from weak, short-range effects. Using nonoriented diffraction patterns with a tomographic scan of the reciprocal space, ADT provides almost complete and pseudo-kinematic reflection intensities from a single nanocrystal and allowed unraveling the tilt structures of $WO_{3-x}F_x$. ADT data was collected from the same "single crystal" (50–200 nm in diameter) in both, static and precession electron diffraction (PED) mode with a probe size of 200 nm in diameter within a tilting range from –60° to +60° resp. –45° to +45° using tilt steps of 1°. Lattice parameters were extracted from the nonprecession data (Table 2), the precession data were used for structure determination. For $WO_{2.90}F_{0.10}$, 12 NED data sets were analyzed (Table S1, Supporting Information). The unit cell could be identified as orthorhombic with three different cell parameters (Table S1, Supporting Information), two being similar, but with distinguishably different size, better detectable in powder XRD (Table 2). The calculated average values of these parameters could be used to index the PXRD data. A full symmetry determination from the systematic absences in the ADT data was not possible due to two main problems: i) The presence of very small (<20 nm) and just slightly differently oriented domains (mosaicity), as confirmed by HRTEM images (Figure 8, vide infra) and/or domains which are 90° rotated against each other with respect to the *c* axis (twin structure). ii) With a density of ≈7.3 g cm^{-3} and a projected particle diameter between 50 and 200 nm, the expected dynamical effects are relatively large.

These two problems ensure that the presence of the reflections (*hk*0: $h + k = 2n$; *h*0*l*: $h + l = 2n$; 0*kl*: $k + l = 2n$) are related only to the crystal structure and exclude any face or body centering. Indexing and analysis of powder XRD data led to the space group *Pbcn* (No. 60; systematic absences 0*kl*: $k = 2n + 1$; *h*0*l*: $l = 2n + 1$; *hk*0: $h + k = 2n + 1$).

An ab initio structure model from powder XRD data was derived with the software EXPO. Possible crystal structures were checked by a rigid body structure refinement with WO_6 octahedra using the TOPAS software package. The atomic parameters were refined from full profile fits of the PXRD data using TOPAS Academic 6.0 by applying the fundamental parameter approach.[34,35]

The refined structure (ReO_3 related, with tilted WO_6 octahedra, derived from the cubic ReO_3 aristotype structure, **Figure 3**A,B) was used as a starting model for a dynamical refinement[37,38] based on four datasets by applying for each dataset a twinning matrix of (010; –100; 001). Three of four twin

Table 2. Dynamical refinement of $WO_{2.58}F_{0.42}$ and $WO_{2.90}F_{0.10}$ against ADT data.

	$WO_{2.58}F_{0.42}$	$WO_{2.90}F_{0.10}$			
Crystal data					
Chemical formula	$WO_{2.58}F_{0.42}$	$WO_{2.90}F_{0.10}$			
Crystal system, space group	cubic, *Pm*-3*m*	orthorhombic, *Pbcn*			
a (Å), *b* (Å), *c* (Å), *V* (Å^3)	3.8143(11), 55.49(3)	7.3435(15), 7.7253(15), 7.4228(12), 421.10(14)			
Z	1	8			
Calculated density [g cm^{-3}]	6.98	7.32			
Data collection					
Radiation type	electrons, 300 kV	electrons, 300 kV			
Wavelength [Å]	0.01969	0.01969			
Precession angle (deg.)	1.0	1.0			
1Projected crystal dimensions [nm^2]	50 × 40	π*100^2			
Average crystal thickness (refined, nm)	20.8	40.2	30.4	20.8	25.3
Resolution (Å)	0.625	0.714			
Tilt step (deg.)	1	1			
No of frames	84	91	88	119	121
Completeness (%)	100	72	63	42	71
No. of used reflections (obs/all)	975/1057	3403/4715	2752/4375	2338/5613	4361/6122
Dynamical structure refinement					
g_{max}, S_g^{max}(matrix), R_{Sg}, N_{or}	1.8, 0.02, 0.8, 96	1.6, 0.01, 0.6, 96			
R1, wR(F) (obs/all)	7.73/8.87, 9.19/9.26	12.72/18.02, 14.13/14.27			
Goodness of fit (obs)	5.32	5.55			
No. of refined parameters[a)]	7 + 84	28 + 419			
Twinning fraction		0.47	0.49	0.49	0.67

[a)]The projected crystal dimension for $WO_{2.90}F_{0.10}$ was bigger than the area illuminated by the beam (diameter of 200 nm).

fraction parameters converged to ≈50% (Table 1), whereas one twin fraction converged to ≈33%. This is in line with problem 1 (vide supra). Nevertheless, the consequential structure model based on a dynamical refinement confirmed the structure determination based on powder XRD data. It is supported by the small deviations in the atomic coordinates of both models (**Table 3**). All parameters and further information about the dynamical refinement are given in Table 3 Three representative zonal images showing different axis directions are presented in Figure 3C.

The structure of the cubic phase ($WO_{2.40}F_{0.60}$) was solved with Superflip[37–39] and refined dynamically based on ADT data (*R*-value of 8.5%). For an anisotropic (harmonic) refinement of the displacement parameters of tungsten, a significant spatial scattering density distribution could be observed in the difference Fourier synthesis. Only an inharmonic functional description of the anisotropic displacement parameters (ADPs) improved the dynamical refinement significantly (*R* value of 7.5%), possible due to a Jahn–Teller distortion.[40] The density distribution (Figure 3D) of tungsten's nonharmonic ADP was interpreted by a superposition of different tungsten sites. For a further refinement the tungsten site W1 was shared with one additional atom W1′, where the sum of the occupancies of W1 and W1′ was fixed to one. The refinement converged, even with isotropic ADP for the tungsten sites, to a *R*-value of 7.5%.

2.4. Crystal Structure of $WO_{2.90}F_{0.10}$

The crystal structure of $WO_{2.90}F_{0.10}$ can be described as a $WO_{3-x}F_x$ tilt structure with $W(O/F)_6$ octahedra tilted along the b-axis. The tilt pattern corresponds to that of the tungsten oxide high-temperature (*Pbcn*) phase with the Glazer nomenclature $a^0\ b^+\ c^-$ (where $a < c < b$) for perovskites.[41–45] The relations between the unit cells of monoclinic and cubic WO_3 (space groups $P2_1/n$ and $Pm\overline{3}m$) and orthorhombic $WO_{3-x}F_x$ (space group *Pcnb)* are sketched schematically in Figure 3A. Apart from small variations of their length, the cell vectors are related according to $a_m \approx a_o \approx ½\ a_c$; $b_m \approx c_o \approx ½\ a_c$; $c_m \approx b_o \approx ½\ a_c$.

2.5. Local Structure of $WO_{2.92}F_{0.08}$ (Conventional Synthesis), $WO_{2.9}F_{0.1}$ (SPS-Prepared), $WO_{2.58}F_{0.42}$ (Conventional Synthesis), and $WO_{2.40}F_{0.60}$ (SPS-Prepared) by ^{19}F MAS-NMR Spectroscopy

ReO_3-type WO_3 (where the W atoms are in octahedral and the O atoms in linear coordination) was subjected to fluorination as described above. The outcomes are the oxyfluorides $WO_{2.92}F_{0.08}$ (conv.),$WO_{2.9}F_{0.1}$ (SPS) and $WO_{2.58}F_{0.42}$ (conv.), $WO_{2.40}F_{0.60}$ (SPS) (**Figure 4**B). Depending on the degree of fluorination, a W atom can be coordinated statistically by five O atoms (maximum six), one or two fluorine atoms (more

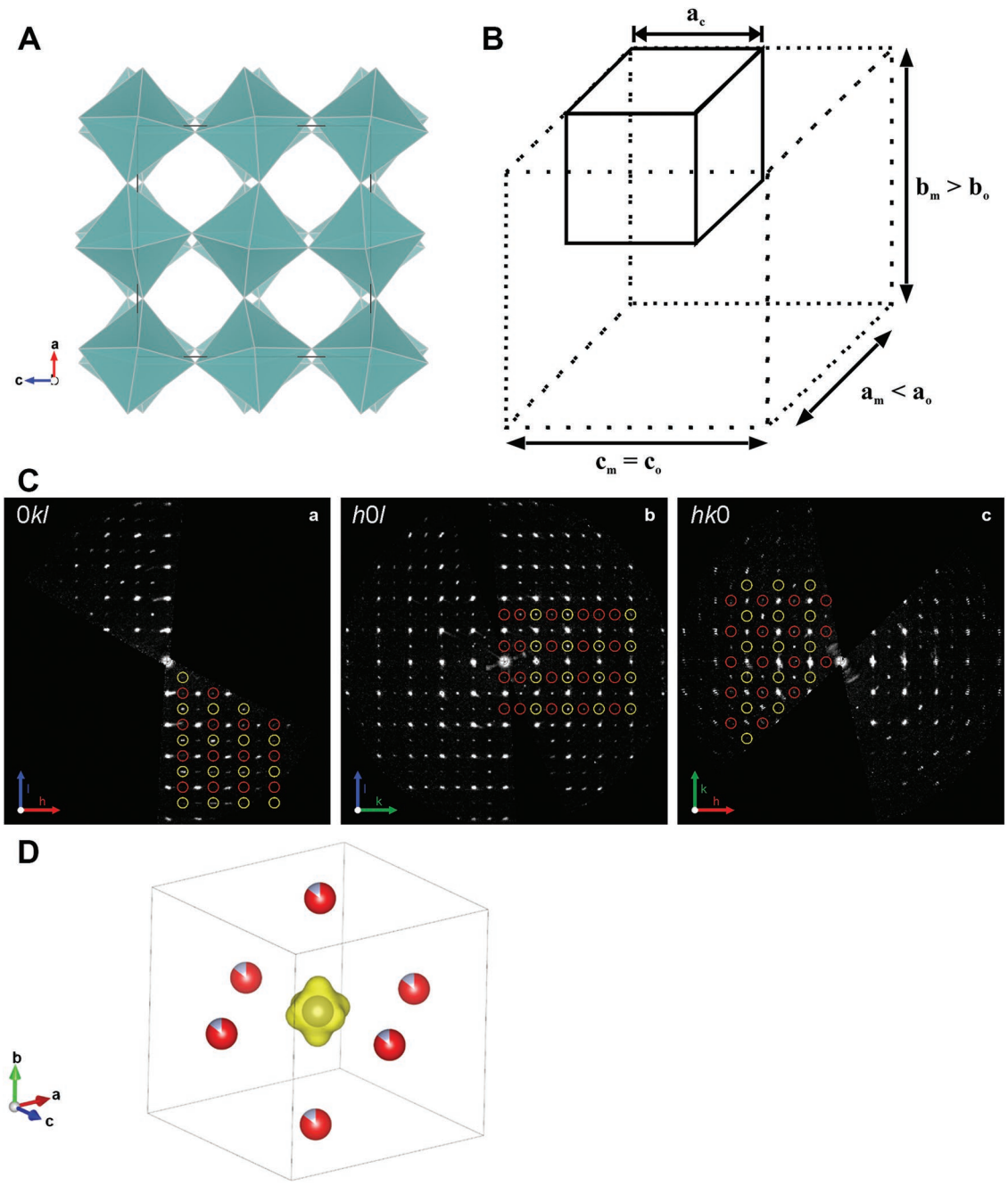

Figure 3. A) View of the orthorhombic $WO_{3-x}Fx$ structure with tilted WO_6 octahedra along the *b*-axis. The tilt pattern corresponds to that of the tungsten oxide high-temperature (*Pbcn*) phase with the Glazer nomenclature $a^0 b^+ c^-$ (where $a < c < b$). B) Relation of the monoclinic, orthorhombic and cubic $WO_{3-x}F_x$ lattices. C) Reconstruction of zonal extinctions from ADT measurements. From left to right: *a*–0*kl*, *b*–*h*0*l*, *c*–*hk*0. Exemplary reconstructed crystallographic zonal patterns from ADT measurements. Bragg reflections in yellow and red circles are forbidden due to the extinctions derived from space group Pbcn. The presence of the Bragg reflections marked in yellow could be explained by twinning. D) Probability density function (in yellow) of the nonharmonic (Gram–Cherlier-expansion) tungsten ADP of the cubic phase dynamically refined against the ADT data. Partly red and blue spheres represent the oxygen fluorine atom sites, respectively.

F neighbors are possible, but statistically not feasible, minimum zero F neighbors) or a vacancy. The ^{19}F MAS NMR spectra of $WO_{3-x}F_x$ recorded at 25 kHz MAS display three (orthorhombic) to four (cubic) resonances. The spectra are discussed in terms of resonance frequency and full width at half height (fwhh) (**Table 4** and Figure 4 and Figure S4, Supporting Information). The resonance frequency (peak position) provides information about the fluorine environment. The line width (fwhh) is a measure for the uniformity of the local field, resp. for the local order. Higher disorder at a particular crystallographic site contributes to broader resonances (fwhh increases).

Table 3. Atomic positions (fractional units) of the $WO_{2.90}F_{0.10}$ structure refined against XRPD and ADT data.

Site	Rietveld refinement			Distance	Dynamical refinement		
	x	*y*	*z*	*d*	*x*	*y*	*z*
W1	−0.246	0.216	−0.490	0.01151	−0.247	0.216	−0.490
O1[a)]	−0.002	0.214	0.034	0.03692	0.000	0.212	0.030
O2[a)]	−0.287	0.990	−0.497	0.05553	−0.291	0.996	−0.499
O3[a)]	−0.218	0.255	−0.246	0.08223	−0.212	0.247	−0.248

[a)]Superposition of O/F in the ratio determined by potentiometry.

For octahedral complexes of the form ($WX_{6-n}F_n$) the substituent effects in solution follow an addition relationship expressed by the equation[46]

$$\delta_F = \delta_F^0 + pC + qT \quad (1)$$

where δ_F^0 represents the chemical shift for WF_6^{2-}, p and q are the numbers of substituents in *cis* and *trans* positions relative to the observed F nucleus, and C and T are shift increments for the *cis* and *trans* substitution, derived from the data for a series of compounds $WX_{6-n}F_n^{2-}$. The base value for δ_F^0 is +165, which corresponds to the chemical shift for WF_6. The electronegativity of the elements building the crystal lattice plays an important role for the electron density around fluorine (with the highest electronegativity according to the Pauling/Hoffmann scales[47,48]) and the ^{19}F chemical shift as well. The difference in electronegativity between W and F is 1.62, which places the W—F bond at the borderline between polar covalent and ionic bonding. According to the same notation the W—O bond is a polar covalent bond (the difference is 1.08) because oxygen is less electronegative than fluorine. Thus, the presence of more oxygen in the surroundings of fluorine (in the WO_3 crystal lattice) would increase the electron density around fluorine and shift the ^{19}F chemical shift to higher fields. At the same conditions the presence of more fluorine in such an environment would lead to less shielding of a fluorine atom and induce a low field shift of its resonance.

The ^{19}F spectra and the corresponding deconvolution of the SPS-prepared (orthorhombic $WO_{2.90}F_{0.10}$-Figure 4A) and conventionally synthesized ($WO_{2.92}F_{0.08}$-Figure 4B) and those of the SPS-prepared (cubic $WO_{2.40}F_{0.60}$-Figure 4C) and conventionally synthesized ($WO_{2.58}F_{0.42}$-Figure 4D) structures are presented in Figure 4. The shifts and the fwhh of the deconvoluted signals are summarized in Table 4.

Three fluorine resonances are detected for the orthorhombic structures at ≈−105, −112 and −139. We attribute the signals at −105 ppm (SPS) and −106 ppm (conventional) with comparable fwhh of ≈4100 Hz to the FW_2O_{10} environment. The resonances at ≈−112 ppm in both orthorhombic structures are probably related with the FW_2O_9F environment (fwhh of ≈1400 Hz). Additionally, signals (fwhh of 1800 and 9400 Hz in both cases) are observed at −138 and −139.6 ppm. They are assumed to be associated with environments around the detected fluorine containing more than one other fluorine atom. This would explain the significant inhomogeneous broadening observed in the ^{19}F spectrum also related with different possible orientations of the fluorine atoms. The conventional synthesis (duration: 36 h) leads to an equilibrium structure with a random ligand distribution around the W atoms, whereas the SPS preparation (duration: a few minutes) favors a trapping of nonequilibrium

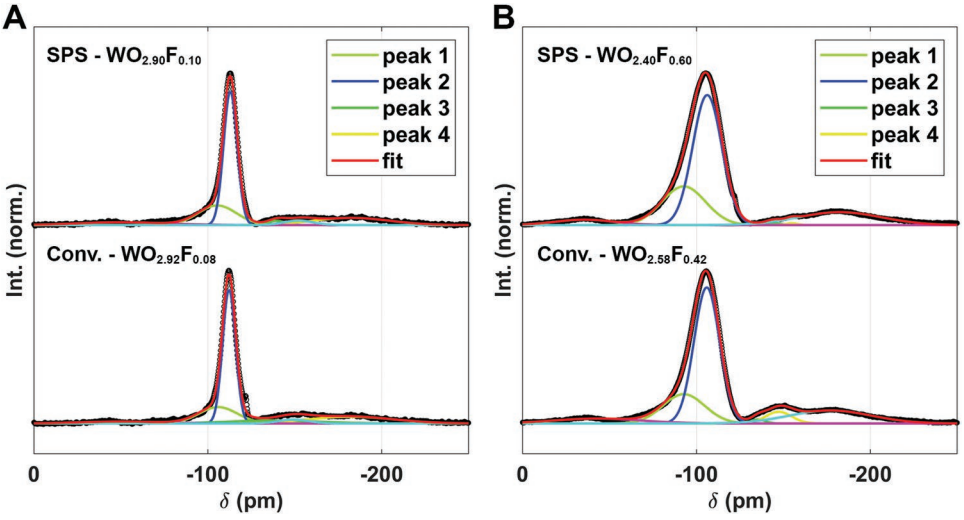

Figure 4. ^{19}F MAS-NMR spectra of orthorhombic A) $WO_{2.90}F_{0.10}$ and cubic B) $WO_{2.58}F_{0.42}$/$WO_{2.40}F_{0.60}$. In each figure the top spectrum is derived from a SPS-prepared sample, while the spectrum at the bottom was obtained from a conventionally prepared sample of comparable composition. The nonfitted peak areas at −180 and −50 ppm belong to spinning side bands.

Table 4. Assignment of the ^{19}F MAS-NMR signals for orthorhombic and cubic $WO_{3-x}F_x$.

SPS/orthorhombic (Figure 4A)	Peak 1	Peak 2	Peak 3	Peak 4
Peak position/ppm	−105.4	−113.0	−139.6.0	
FWHM/kHz	4.2	1.5	4.9	
Relative peak area	29%	69%	3%	
Conv./ orthorhombic (Figure 4A)				
Peak position/ppm	−106.0	112.2	138.0	
FWHM/kHz	4.1	1.4	9.4	
Relative peak area	24%	66%	10%	
SPS/cubic (Figure 4B)				
Peak position/ppm	−92.7	−106.2	−144.3	−154.8
FWHM/kHz	4.7	3.2	1.5	1.2
Relative peak area	31%	69%	1%	1%
Conv./cubic (Figure 4B)				
Peak position/ppm	−92.8	−106.0	−135.5	−147.3
FWHM/kHz	4.5	2.8	1.5	2.8
Relative peak area	24%	69%	1%	6%

states and local ordering effects. The smaller fwhh observed for the SPS-prepared samples is assumed to arise from the fast reaction at the surface of the WO_3 particle grains.

The spectra of the cubic structures exhibit four signals. The resonances at ≈−92.7 ppm (FW_2O_{10}) and −106 ppm (FW_2O_9F) are well defined in both, conventionally synthesized and SPS-prepared samples. The fwhh are comparable in both cases, but they are slightly broadened for the SPS-prepared samples with 200 to 400 Hz. The other low intensity resonances in both cases cover a range of −135 to −154 ppm. They are probably associated with higher fluorine environments at the contact border between WO_3 and PTFE. The fwhh vary between 1200 and 2800 Hz. A calculated degree of fluorination for the cubic samples ($x = 0.45$ and 0.60) corresponds statistically to 1.5 fluorine atoms in two interconnected octahedra. This matches the relative area of the second peak for both cubic samples at ≈50%. For higher amounts of fluorine in the cubic structures, the SPS reaction leads to a higher local fluorine content while the conventional reactions leads to a slightly more uniform product (the fwhh for the SPS reaction are broader for both). These assignments are supported by the calculated ^{19}F δ_{iso} values of F atom environments in NbO_2F (−62, −53, −43, and −30 ppm)[27] and TaO_2F (−84, −73, −62, and −46 ppm).[27]

A SEM image of the polished pellet surface (**Figure 5**A) shows the formation of a dense product with a macroscopic uniform elemental distribution over the pellet cross-section which confirms the presence of one single phase product (as shown by X-ray diffraction). Both, TEM and SEM images reveal the grains to be randomly oriented, without pronounced morphology and with a large size distribution, most likely due to ball-milling treatment of the starting materials. TEM-analysis reveals a less pronounced grain growth during SPS compared to conventional synthesis (Figure S5, Supporting Information) and the formation of more uniform grains after SPS. The observed porosity is caused most likely by the evaporation of decomposed PTFE because incomplete mixing leads to larger the formation of cavities and remnants of PTFE (Figure S1B, Supporting Information).

2.6. Electronic Structure and Composition of Cubic $WO_{3-x}F_x$ by XPS Spectroscopy

Figure 6A–D shows the W 4f, F 1s, O 1s, and C 1s regions of the XPS spectra of cubic $WO_{3-x}F_x$ synthesized by SPS and conventionally, before carbon removal, together with a the spectra of a ball-milled and SPS treated WO_3 (99+%, ChemPur). The

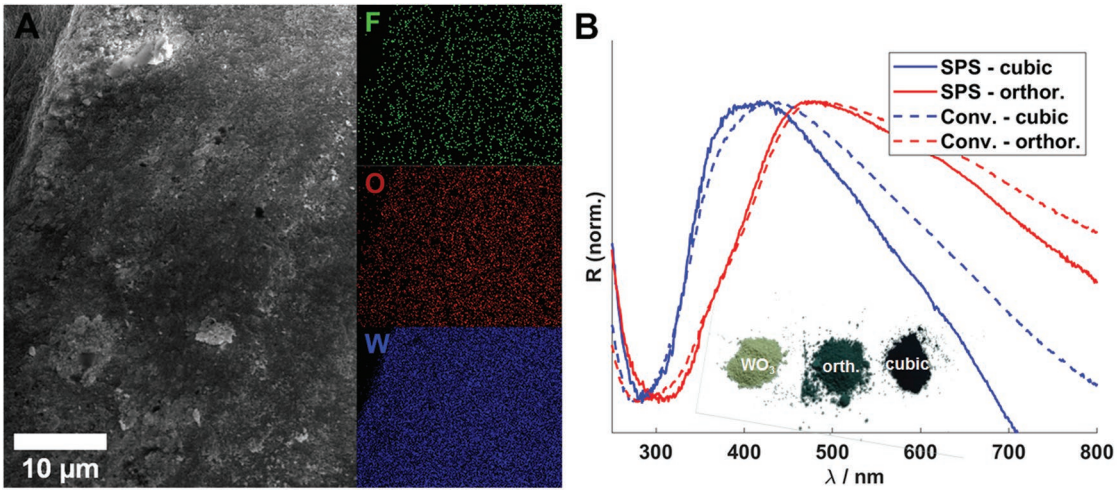

Figure 5. A) SEM-EDX image of a cross-section of a SPS-pellet of cubic $WO_{2.4}F_{0.6}$. Cavities are caused by evaporation of decomposed PTFE. B) Diffuse reflectance UV–vis spectra of cubic and orthorhombic conventionally prepared $WO_{3-x}F_x$ (blue – $WO_{2.58}F_{0.42}$, red – $WO_{2.92}F_{0.08}$, dotted lines) and by SPS-prepared (blue – $WO_{2.40}F_{0.60}$, red – $WO_{2.90}F_{0.10}$, solid lines).

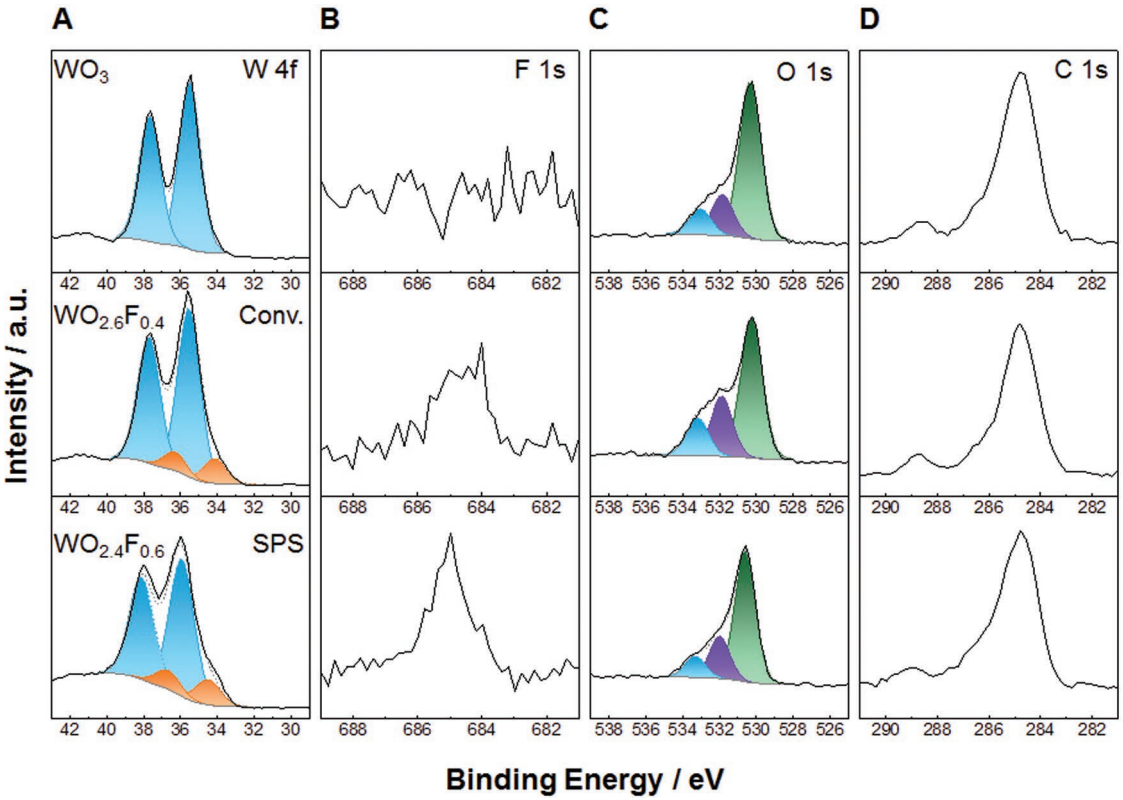

Figure 6. XPS sub-spectra of A) W 4f, B) F 1s, C) O 1s, D) and C 1s of reference WO_3 (top) cubic $WO_{3-x}F_x$ prepared conventionally (middle) and by SPS (bottom). All spectra were calibrated by the C 1s signal and fitted considering the spin-orbit splits for each element.

peaks centered at 36 and 38 eV (Figure 6A) are assigned to the W 4f 7/2 and W 4f 5/2 orbitals, respectively. They are characteristic for the oxidation state +6 for WO_3 and $WO_{3-x}F_x$. The spectra of cubic $WO_{3-x}F_x$ show significant shoulders at 34 and 36 eV, which indicate the presence of W^{5+}. The distinct shoulder in the W 4f region and the stronger signal in the F 1s region of SPS-prepared $WO_{2.4}F_{0.6}$ confirm the presence of fluorine and W^{6+}/W^{5+} as expected for a higher degree of fluorination. The XPS spectra of the F 1s core electrons (Figure 6B) show a single, weak signal centered at 684–685 eV, originating from W—F bonds on the surface of the tungsten oxyfluoride samples. The O 1s regions (Figure 6C) show three signals at ≈530, 532, and 533 eV, which can be assigned to lattice oxide, surface hydroxide groups and adsorbed water. Since these samples were not heated in air after synthesis, the C 1s region shows a strong signal, indicating the presence of carbon from Teflon remnants and additional surface-bound carbonate. The XPS overview spectrum and the spectra after heating in air in Figures S6 and S7 (Supporting Information) confirm the complete removal of carbon and the presence of W, O, and F together with adsorbed water species.

2.7. Photocatalytic Properties

The optical bandgaps were derived from the equation: $(F(R)\ h\nu)^n = B(E - E_g)$, where $F(R)$ is the Kubelka–Munk function, $h\nu$ the photon energy, B a constant, and n is 2 or 1/2 for direct or As shown in Figure 5B (vide supra), orthorhombic and cubic $WO_{3-x}F_x$ exhibit an intense absorption between 470 and 600 nm, suggesting that the light absorption for photocatalysis mainly derives from the visible part of the spectrum. The absorption edge is blue-shifted compared to the tungsten bronze $W_{18}O_{49}$.[50] Indirect transitions, respectively.[49] Energy gaps (E_g) of 3.2 and 3.5 eV were derived by extrapolating the linear region of $(Ah\nu)^{1/2}$ to $h\nu = 0$.

To understand the relationship between the tungsten oxyfluoride composition and its photocatalytic performance, the activity of SPS- and conventionally prepared samples was evaluated by the photocatalytic decomposition of the model substrate Rhodamin B (RhB) in aqueous solution under visible light (blue light LED, 18 W). The temporal evolution of UV–vis absorption spectra of RhB solution in the presence of $WO_{2.92}F_{0.08}$ and $WO_{2.58}F_{0.42}$ prepared by conventional solid state chemistry, (A, B) and $WO_{2.90}F_{0.10}$ and $WO_{2.40}F_{0.60}$ prepared by SPS (C, D) under blue light irradiation is displayed in **Figure 7**A–D and Figure S11 (Supporting Information), where the decrease of the absorption at 554 nm with exposure time is related to the concentration of RhB in solution. Figure 7 shows that only 10% of RhB are degraded by both, $WO_{2.92}F_{0.08}$ and $WO_{2.58}F_{0.42}$ (prepared conventionally), while 25% and 70% are degraded by $WO_{2.90}F_{0.10}$ and $WO_{2.40}F_{0.60}$ (prepared by SPS). The linear plots of (c_0/c) versus irradiation time (t) suggest a pseudo-first order kinetics. The rate constants are given in Figure S7 (Supporting Information). The photocatalytic activities of SPS-prepared $WO_{2.90}F_{0.10}$ and $WO_{2.40}F_{0.60}$ are much

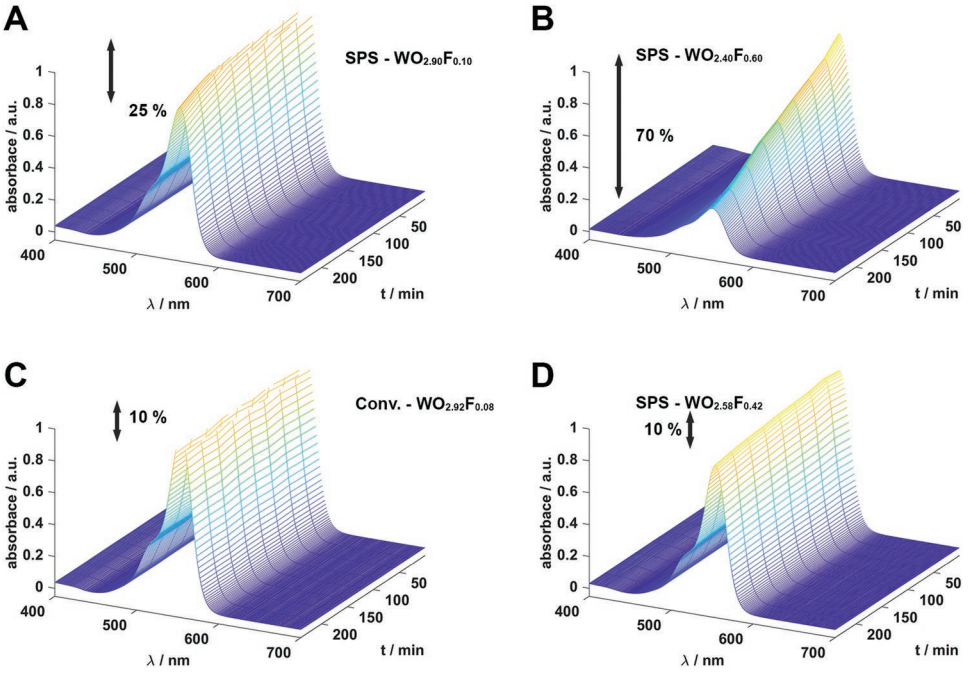

Figure 7. UV–vis spectra showing the photocatalytic degradation of RhB in aqueous solution for $WO_{2.92}F_{0.08}$/$WO_{2.90}F_{0.10}$ A,C) and $WO_{2.58}F_{0.42}$/$WO_{2.40}F_{0.60}$ D,B). Data in the upper row A,B) was obtained by the SPS compound, while C,D) were prepared by conventional solid state chemistry. Rate constants (Figure S10, Supporting Information): $WO_{2.90}F_{0.10}$ –0.29 μM min^{-1}; $WO_{2.40}F_{0.60}$ –0.59 μM min^{-1}; $WO_{2.92}F_{0.08}$ –0.03 μM min^{-1}; $WO_{2.58}F_{0.42}$ –0.09 μM min^{-1}.

higher than those of samples prepared by conventional reactions. The activities of $WO_{2.92}F_{0.08}$ and $WO_{2.58}F_{0.42}$ (prepared conventionally) and $WO_{2.90}F_{0.10}$ and $WO_{2.40}F_{0.60}$ (prepared by SPS) are dictated by the dye adsorption, the light absorption for electron–hole generation, and electron–hole separation. Therefore, we investigated the effect of RhB adsorption on $WO_{2.92}F_{0.08}$/$WO_{2.90}F_{0.10}$ and $WO_{2.58}F_{0.42}$/$WO_{2.40}F_{0.60}$. Aliquots of the respective oxyfluorides were added to 5 mL of RhB solution (0.2 mmol L^{-1}), and the solutions were stirred in the dark for 240 min to reach the adsorption–desorption equilibrium. The intensity of the RhB absorption band in the presence of $WO_{2.92}F_{0.08}$/$WO_{2.90}F_{0.10}$ and $WO_{2.58}F_{0.42}$/$WO_{2.40}F_{0.60}$ decreases with increasing adsorption time under dark condition (Figure S9, Supporting Information). Figure S9 (Supporting Information) shows that ≈2% (for $WO_{2.90}F_{0.10}$) and 10% (for $WO_{2.40}F_{0.60}$) of RhB were removed within 3 h in the dark, i.e., $WO_{2.90}F_{0.10}$ and $WO_{2.40}F_{0.60}$ have a low dye adsorption capacity. While the Brunauer/Emmett/Teller (BET) surface areas of the samples (≈10–12 m^2 g^{-1}) are comparable, an increase in the fluorine content results in a much darker color and higher conductivity. The visible light absorption of $WO_{3-x}F_x$ may be associated with electronic transitions from i) the valence band to (localized) polaron states, ii) from polaron states to the conduction band or iii) by electron hopping between W^{5+} and W^{6+} sites.[51,52] The much higher photocatalytic activity of the SPS-prepared samples ($WO_{2.90}F_{0.10}$ and $WO_{2.40}F_{0.60}$) is attributed to combined effects of smaller domain size (Figure S5, Supporting Information), a lower degree of ordering, a higher number of defect sites at the domain surfaces and additional twin boundaries (**Figure 8**) and to the presence of F surface

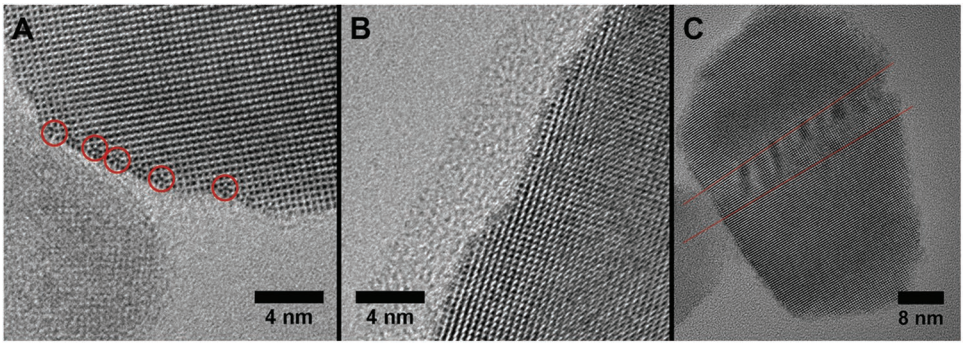

Figure 8. A–C) TEM (HRTEM) images acquired with underfocus (black atom contrast) of a SPS-prepared A) and conventionally prepared B) samples of cubic $WO_{2.40}F_{0.60}$.The ReO_3-type structure can easily be seen. The HRTEM images also show the lower ordering at the particle surface for the SPS-prepared sample in comparison with a conventional sample. C) HRTEM image of an SPS-prepared particle with twin boundaries.

sites (lower adsorption of dye due to the lower polarizability of fluorine).

3. Conclusion

We have shown that reactions using SPS allow the high-speed solid state fluorination of WO_3 using poly(tetrafluoroethylene) in large quantities. The degree of fluorination is very high and comparable to that achieved with hydrofluoric acid under hydrothermal conditions in sealed gold ampoules. The reactions times could be reduced by more than 2 orders of magnitude from 2 days to a few minutes and do not require toxic and caustic chemicals. The structure and composition of the resulting tungsten oxyfluorides, $WO_{2.90}F_{0.10}$ and $WO_{2.40}F_{0.60}$, was determined by a combination of F^--potentiometry, X-ray powder diffraction, automated electron diffraction tomography, ^{19}F MAS-NMR, XPS, HRTEM, and SEM/EDX. The rapid SPS transformations presumably involve F^- anion transport in the applied electric field. The fast SPS reaction leads to the formation of nonequilibrium micro- and surface structures with different levels of metastability. Thus, the SPS-derived oxyfluorides $WO_{3-x}F_x$ yield–different from the bulk phases obtained by conventional high-temperature reactions–monoliths of metal oxide fluoride nanoparticles with trap states associated with surface defects that lead to high photocatalytic activity. The high potential of this new synthetic SPS approach is that i) mixed-valent tungsten oxide fluorides $WO_{3-x}F_x$ ($0 < x < 0.60$) are obtained within minutes, without toxic chemicals and in copious amounts and, ii) the degree of fluorination is increased. iii) Importantly, the chemical reactivity of the SPS-derived oxyfluorides $WO_{3-x}F_x$ differs significantly from that of products obtained by conventional solid state reaction. This study is a proof of concept for the development of cheap and functionally efficient materials from PTFE polymer. It even allows a reutilization of PTFE polymer scrap for the synthesis of valuable tungsten oxyfluorides through SPS processing.

4. Experimental Section

Synthesis: Tungsten trioxide (99+%, Chempur) and poly(tetrafluoroethylene) (PTFE, Sigma-Aldrich, 1 µm powder) were weighed in their respective molar ratios, ball-milled (Fritsch Pulverisette) for 5 h in ethanol and dried by centrifugation and drying overnight at 70 °C in a drying chamber. The preparation is illustrated in Figure 1A (vide supra). WO_3 and PTFE were used in stoichiometric amounts as precursors for both conventional and SPS synthesis. SPS yielded dense pellets of products $WO_{3-x}F_x$ in a single step according to the representative reaction $4WO_3 + (C_2F_4)_n = 4WO_{3-n}F_n + 2nCO_2$.

For SPS preparation, samples containing ≈2.5 g of the powder mixtures were enclosed with graphite foil and placed in graphite dies. The dies were put subsequently into an SPS HP D 25 (FCT-systems) and heated up to 550 °C with 50 °C min^{-1} and kept at this temperature for 6 min (p = 19 MPa). To achieve a higher densification, an additional heating step at 700 °C was added to the reaction process (p = 50 MPa). All samples were annealed for additional 3 h at 400 °C in air to remove remnants of carbon resulting from the decomposition of PTFE. Reference samples for conventional high temperature reactions were prepared by placing powder mixtures (≈500 mg) in evacuated quartz ampules and heating for 36 h at 550 °C.[22]

X-Ray Powder Diffraction Analysis: Samples for X-Ray diffraction were prepared on polyvinylacetate foil. Diffractograms were obtained using a STOE Stadi P powder diffractometer, equipped with a Mythen 1k detector using Mo$K\alpha_1$ radiation. The sample was measured in transmission in 0.015° steps (continuous scan, 150 s per degree) covering a 2θ range from 1.5° to 73.4°. Rietveld refinement[34] was performed with Topas Academic V6 using the fundamental parameters approach.[35] The structures of the crystalline phases were determined by ADT.

High-resolution synchrotron powder diffraction data were collected at beamline 11-BM at the Advanced Photon Source (APS), Argonne National Laboratory using a wavelength of λ = 0.41385 nm. Data were fit using TOPAS Academic V6 program suite, using the fundamental parameter approach.[35]

Scanning Electron Microscopy (SEM): Field-emission scanning electron microscopy was performed on a NOVA Nano-SEM with an attached Oxford Inca X-ray system for chemical analysis. The obtained SPS pellets were cut and polished to obtain cross-sectional pieces. Secondary and backscattered electron images were collected with acceleration voltages of 5 keV and 15 or 20 keV for EDX mapping, respectively.

X-Ray Photoelectron Spectroscopy: Measurements were carried out using a PHI5000 Versa Probe II with an Al anode. The probed surface area was 100 µm × 1400 µm (i.e., X-ray spot size), and an X-ray power of 100 W was used. The pass energy of the analyzer was set to 23.5 eV for detailed spectra and to 187.9 eV for survey scans. All spectra were charge corrected to a binding energy of 284.8 eV for the C 1s line corresponding to adventitious aliphatic carbon. Measurements were evaluated using the CasaXPS software.

Transmission Electron Microscopy: Powdered samples were prepared by placing one drop (10 µL) of a diluted NP solution in ethanol (0.1 mg mL^{-1}) on a carbon-coated copper grid and by letting it dry at room temperature for transmission electron microscopy, High-resolution TEM (HRTEM), electron dispersive X-ray spectroscopy (EDXS) and automated electron diffraction tomography investigations. TEM, HRTEM, EDX and ADT measurements were carried out with a FEI TECNAI F30 S-TWIN transmission electron microscope equipped with a field emission gun and working at 300 kV. TEM images and nano electron diffraction (NED) patterns were taken with a CCD camera (16-bit 4.096 × 4.096 pixel GATAN ULTRASCAN4000) and acquired by Gatan Digital Micrograph software. Scanning transmission electron microscopy (STEM) images were collected by a FISCHIONE high-angular annular dark field (HAADF) detector and acquired by Emispec ES Vision software.

Automated Electron Diffraction Tomography: 3D electron diffraction data were collected using an automated acquisition module developed for FEI microscopes.[53] For high tilt experiments all acquisitions were performed with a FISCHIONE tomography holder. A condenser aperture of 10 µm and mild illumination settings (gun lens 8, spot size 6) were used in order to produce a semi-parallel beam of 200 nm in diameter on the sample (115 e^- nm^{-2} s^{-1}). Crystal position tracking was performed in microprobe STEM mode and NED patterns were acquired sequentially in steps of 1.0°. Tilt series were collected within a total tilt range up to 120° resp. 90°, occasionally limited by overlapping of surrounding crystals or grid edges. ADT data were collected with electron beam precession (precession electron diffraction, PED).[54] PED was used in order to improve reflection intensity integration quality.[55] PED was performed using a Digistar unit developed by NanoMEGAS SPRL. The precession angle was kept at 1.0°. The eADT software package was used for 3D electron diffraction data processing.[56] Ab initio structure solution was performed assuming the kinematic approximation $I \approx |F_{hkl}|^2$. Scattering factors for electrons were taken from Doyle and Turner.[57] The data were processed using the software packages PETS[58] and JANA2006[59] for dynamical refinement.[36] The relevant information on the crystal structure determination by ADT is compiled in Table 1.

Brunauer/Emmett/Teller sorption: BET measurements were conducted using the gas adsorption setup Autosorb-6B from Quantachrome with nitrogen as analysis gas. The temperature during the measurements was 77 K. Data evaluations were conducted with the software Quantachrome ASiQWin 3.0.

UV–Vis Spectroscopy: Ultraviolet–visible (UV–vis) reflectance spectra ranging from 200 to 800 nm were collected on a Cary 5G UV–vis–NIR spectrophotometer using an Ulbricht sphere. $BaSO_4$ was used as white standard. The samples were measured by mixing a few mg of powder with $BaSO_4$ and pressing the mixture into a pellet.

Nuclear Magnetic Resonance (NMR) Spectroscopy: All solid-state NMR experiments were recorded on a Bruker Avance 400 DSX spectrometer at ^{19}F frequency of 376.25 MHz. A two-channel commercial Bruker 2.5 mm probe head at spinning speeds of 25 kHz was used for the ^{19}F direct excitation measurements. No changes in the spectra are expected at slightly elevated temperatures, so no temperature correction for the frictional heating due to the sample rotation has been performed. All spectra are background corrected.

Fluorine-Ion Selective Electrode Measurements: F^--ion selective potentiometric measurements were carried out using an F^-ion-selective electrode and a Titrando 907, both from Metrom. 15–30 mg of the sample powders were dissolved in 25 mL 1.2 M NaOH solution and then neutralized with 1.2 M HCl solution. The solution then was transferred into 100 mL volumetric flasks and filled with TISAB IV (Bernd Kraft) solution. 40 mL of each mixture were used to determine the fluorine content by comparison of the measured potential with an external standard calibration. Standard solutions with the concentrations 0.2, 0.40, 1.0, and 2.50 mmol L^{-1} were obtained by diluting a 0.1 mol L^{-1} NaF standard solution. The standard was prepared by dissolving 95 mg NaF (99,0% pa, Fluka) in 50 mL of deionized water.

Photocatalytic Activity of $WO_{3-x}F_x$: $WO_{3-x}F_x$ particles (SPS- and conventionally prepared) were suspended in distilled water (1 mg mL^{-1}), and their photocatalytic activity was explored against the model substance Rhodamine B (RhB). Freshly prepared aqueous dispersions of $WO_{3-x}F_x$ nanoparticles (1 mg mL^{-1}) were mixed with the model compound RhB (0.1 mg mL^{-1}) and irradiated using 6 light-emitting diodes from Osram OSLON SSL 80 with peak emission at 451 nm (deep blue) driven by constant current 350 mA in series connection. The experiments were carried at room temperature as follows: The mixture was exposed for 4 h to the LEDs after equilibration time of 30 min. A 400 µL aliquot was taken every 30 min, centrifuged and 60 µL of the clear solution were diluted with 940 µL distilled water. The UV–vis spectrum was recorded using a Cary 5G UV–vis–NIR spectrophotometer (Varian Inc., Palo Alto, CA, USA). As control, a solution of RhB (0.1 mg mL^{-1}) and $WO_{3-x}F_x$ nanoparticles (1 mg mL^{-1}) was treated in the dark under otherwise identical experimental conditions. The calculations (C/C_0) were performed considering a wavelength value of 554 nm–the maximum of the RhB UV–vis spectral band.

Supporting Information

Supporting Information is available from the Wiley Online Library or from the author.

Acknowledgements

M.A.L. is recipient of a Carl-Zeiss-fellowship. This research was supported by a grant from the Deutsche Forschungsgemeinschaft within the priority program Manipulation of Matter Controlled by Electric and Magnetic Fields: Towards Novel Synthesis and Processing Routes of Inorganic Materials (SPP 1959). Use of the Advanced Photon Source at Argonne National Laboratory was supported by the U.S. Department of Energy, Office of Science, Office of Basic Energy Sciences, under Contract No. DE-AC02-06CH11357.

Conflict of Interest

The authors declare no conflict of interest.

Author Contributions

All authors have given approval to the final version of the manuscript.

Keywords

automated diffraction tomography, fluorination, photocatalysis, spark plasma synthesis, tungsten oxyfluoride

Received: October 31, 2019
Revised: December 9, 2019
Published online: February 12, 2020

[1] D. M. P. Mingos, D. R. Baghurst, *Chem. Soc. Rev.* **1991**, *20*, 1.
[2] H. J. Kitchen, S. R. Vallance, J. L. Kennedy, N. Tapia-Ruiz, L. Carassiti, A. Harrison, A. G. Whittaker, T. D. Drysdale, S. W. Kingman, D. H. Gregory, *Chem. Rev.* **2014**, *114*, 1170.
[3] O. Guillon, C. Elsässer, O. Gutfleisch, J. Janek, S. Korte-Kerzel, D. Raabe, C. A. Volkert, *Mater. Today* **2018**, *21*, 527.
[4] O. Guillon, J. Gonzales-Julian, B. Dargartz, T. Kessel, G. Schierning, J. Räthel, M. Herrmann, C. Sässer, O. Gutfleisch, J. Janek, S. Korte-Kerzel, D. Raabe, C. A. Volkert, *Adv. Eng. Mater.* **2014**, *16*, 830.
[5] R. Orru, R. Licheri, A. M. Locci, A. Cincotti, G. Cao, *Mater. Sci. Eng., R* **2009**, *63*, 127.
[6] Z. A. Munir, U. Anselmi-Tamburini, M. Ohyanagi, *J. Mater. Sci.* **2006**, *41*, 763.
[7] H. Yoshida, K. Morita, K. Soga, *J. Ceram. Soc. Jpn.* **2016**, *124*, 932.
[8] M. Joos, G. Cerretti, I. Veremchuk, P. Hofmann, H. Frerichs, D. H. Anjum, T. Reich, I. Lieberwirth, M. Panthöfer, W. G. Zeier, W. Tremel, *Inorg. Chem.* **2018**, *57*, 1259.
[9] J. R. Friedman, J. E. Garay, U. Anselmi-Tamburini, Z. A. Munir, *Intermetallics* **2004**, *12*, 589.
[10] W. Chen, U. Anselmi-Tamburini, J. E. Garay, J. R. Groza, Z. A. Munir, *Mater. Sci. Eng., A* **2005**, *394*, 132.
[11] C. Recknagel, N. Reinfried, P. Höhn, W. Schnelle, H. Rosner, Y. Grin, A. Leithe-Jasper, *Sci. Technol. Adv. Mater.* **2007**, *8*, 357.
[12] M. Beekman, M. Baitinger, H. Borrmann, W. Schnelle, K. Meier, G. S. Nolas, Y. Grin, *J. Am. Chem. Soc.* **2009**, *131*, 9642.
[13] D. Portehault, V. Maneeratana, C. Candolfi, N. Oeschler, I. Veremchuk, Y. Grin, C. Sanchez, M. Antonietti, *ACS Nano* **2011**, *5*, 9052.
[14] P. R. Slater, J. P. Hodges, M. G. Francesconi, P. P. Edwards, C. Greaves, I. Gameson, M. Slaski, *Phys. C* **1995**, *253*, 16.
[15] S. Rüdiger, E. Kemnitz, *Dalton Trans.* **2008**, 1117.
[16] *Functionalized Inorganic Fluorides: Synthesis, Characterization and Properties of Nanostructured Solids* (Ed: A. Tressaud), John Wiley & Sons, Ltd, New York **2010**.
[17] W. Sleight, *Inorg. Chem.* **1969**, *8*, 1764.
[18] Y. Kamihara, T. Watanabe, M. Hirano, H. Hosono, *J. Am. Chem. Soc.* **2008**, *130*, 3296.
[19] P. R. Slater, *J. Fluorine Chem.* **2002**, *117*, 43.
[20] F. J. Berry, X. Ren, R. Heap, P. R. Slater, M. F. Thomas, *Solid State Commun.* **2005**, *134*, 621.
[21] Y. Kobayashi, M. Tian, M. Eguchi, T. E. Mallouk, *J. Am. Chem. Soc.* **2009**, *131*, 9849.
[22] D. Hirai, E. Climent-Pascual, R. J. Cava, *Phys. Rev. B* **2011**, *84*, 17451.
[23] S. E. Dutton, D. Hirai, R. J. Cava, *Mater. Res. Bull.* **2012**, *47*, 714.
[24] D. Hirai, O. Sawai, T. Nunoura, Z. Hiroi, *J. Fluorine Chem.* **2018**, *209*, 43.
[25] D. Spetter, M. N. Tahir, J. Hilgert, I. Khan, A. Qurashi, H. Lu, T. Weidner, W. Tremel, *ACS Sustainable Chem. Eng.* **2018**, *6*, 12641.

[26] L.-S. Du, F. Wang, C. P. Grey, *J. Solid State Chem.* **1998**, *140*, 285.
[27] J. Dabachi, M. Body, C. Galven, F. Boucher, C. Legein, *Inorg. Chem.* **2017**, *56*, 5219.
[28] C. B. Mo, S. I. Cha, K. T. Kim, K. H. Lee, S. H. Hong, *Mater. Sci. Eng., A* **2005**, *395*, 124.
[29] M. N. Tahir, B. Oschmann, D. Buchholz, X. Dou, I. Lieberwirth, M. Panthöfer, W. Tremel, R. Zentel, S. Passerini, *Adv. Energy Mater.* **2016**, *6*, 1501489.
[30] H. Zhang, Y. Li, Y. Wang, P. Liu, H. Yang, X. Yao, T. An, B. J. Wood, H. Zhao, *J. Mater. Chem. A* **2013**, *1*, 6563.
[31] S. L. Madorsky, S. Straus, D. Thompson, L. Williams, *J. Polym. Sci.* **1949**, *4*, 639.
[32] B. B. Baker, D. J. Kasprzak, *Polym. Degrad. Stab.* **1993**, *42*, 181.
[33] E. E. Lewis, M. A. Taylor, *J. Am. Chem. Soc.* **1947**, *69*, 1968.
[34] H. M. Rietveld, *J. Appl. Crystallogr.* **1969**, *2*, 65.
[35] J. J. Coelho, *J. Appl. Crystallogr.* **2018**, *51*, 210.
[36] I. Vegard, *Z. Phys.* **1921**, *5*, 17.
[37] L. Palatinus, D. Jacob, P. Cuvillier, M. Klementová, W. Sinkler, L. D. Marks, *Acta Crystallogr., Sect. A: Found. Crystallogr.* **2013**, *69*, 171.
[38] L. Palatinus, V. Petricek, C. A. Correa, *Acta Crystallogr., Sect. A: Found. Adv.* **2015**, *71*, 235.
[39] L. Palatinus, G. Chapuis, *J. Appl. Crystallogr.* **2007**, *40*, 786.
[40] R. A. Wheeler, M. H. Whangbo, T. Hughbanks, R. Hoffmann, J. K. Burdett, T. A. Albright, *J. Am. Chem. Soc.* **1986**, *108*, 2222.
[41] A. M. Glazer, *Acta Crystallogr., Sect. B: Struct. Crystallogr. Cryst. Chem.* **1972**, *28*, 3384.
[42] A. M. Glazer, *Acta Crystallogr. A* **1975**, *31*, 756.
[43] P. M. Woodward, *Acta Crystallogr., Sect. B: Struct. Sci.* **1997**, *53*, 44.
[44] D. I. Woodward, I. M. Reanay, *Acta Crystallogr., Sect. B: Struct. Sci.* **2005**, *61*, 387.
[45] R. H. Mitchell, M. D. Welche, A. R. Chakhmouradian, *Mineral. Mag.* **2017**, *81*, 411.
[46] M. Biswal, M. Body, C. Legein, A. Sadoc, F. Boucher, *J. Solid State Chem.* **2013**, *207*, 208.
[47] L. Pauling, *J. Am. Chem. Soc.* **1932**, *54*, 3570.
[48] M. Rahm, T. Zeng, R. Hoffmann, *J. Am. Chem. Soc.* **2019**, *141*, 342.
[49] A. Yella, M. N. Tahir, S. Meuer, R. Zentel, R. Berger, M. Panthöfer, W. Tremel, *J. Am. Chem. Soc.* **2009**, *131*, 17566.
[50] G. Kortüm, *Reflectance Spectroscopy*, SpringerNew York **1969**.
[51] J. A. Duffy, *Bonding, Energy Levels and Bands in Inorganic Solids*, Longman, Harlow, UK **1990**.
[52] G. Kieslich, G. Cerretti, I. Veremchuk, R. P. Hermann, M. Panthöfer, J. Grin, W. Tremel, *Phys. Status Solidi A* **2016**, *213*, 808.
[53] E. Mugnaioli, T. Gorelik, U. Kolb, *Ultramicroscopy* **2009**, *109*, 758.
[54] U. Kolb, T. Gorelik, C. Kübel, M. T. Otten, D. Hubert, *Ultramicroscopy* **2007**, *107*, 507.
[55] R. Vincent, P. A. Midgley, *Ultramicroscopy* **1994**, *53*, 271.
[56] U. Kolb, E. Mugnaioli, T. E. Gorelik, *Cryst. Res. Technol.* **2011**, *46*, 542.
[57] P. A. Doyle, P. S. Turner, *Acta Crystallogr. A* **1968**, *24*, 390.
[58] L. Palatinus, *PETS-Program for Analysis of Electron Diffraction Data*, Institute of Physics, Prague **2011**.
[59] V. Petříček, M. Dušek, L. Palatinus, *Z. Kristallogr.* **2014**, *229*, 345.